

ARTICLE OPEN



Pressure evolution of electron dynamics in the superconducting kagome metal CsV₃Sb₅

Maxim Wenzel¹✉, Alexander A. Tsirlin^{2,3}✉, Francesco Capitani⁴, Yuk T. Chan¹, Brenden R. Ortiz^{5,6}, Stephen D. Wilson⁵, Martin Dressel¹ and Ece Uykur^{1,7}✉

The coexistence of the charge-density wave (CDW) and superconducting phases and their tunability under external pressure remains one of the key points in understanding the electronic structure of AV₃Sb₅ (A = K, Rb, Cs) kagome metals. Here, we employ synchrotron-based infrared spectroscopy assisted by density-functional calculations to study the pressure evolution of the electronic structure at room temperature up to 17 GPa experimentally. The optical spectrum of CsV₃Sb₅ is characterized by the presence of localized carriers seen as a broad peak at finite frequencies in addition to the conventional metallic Drude response. The non-monotonic pressure dependence of this low-energy peak reflects the re-entrant behavior of superconductivity and may be interpreted in terms of electron-phonon coupling, varying with the growth and shrinkage of the Fermi surface under pressure. Moreover, drastic modifications in the low-energy interband absorptions are observed upon the suppression of CDW. These changes are related to the upward shift of the Sb2 $p_x + p_y$ band that eliminates part of the Fermi surface around the *M*-point, whereas band saddle points do not move significantly. These observations shed new light on the mixed electronic and lattice origin of the CDW in CsV₃Sb₅.

npj Quantum Materials (2023)8:45; <https://doi.org/10.1038/s41535-023-00577-4>

INTRODUCTION

Discovered in 2019¹, the non-magnetic kagome metal series AV₃Sb₅ (A = K, Rb, Cs) provides an exciting playground for studying a plethora of fascinating electronic phenomena, including the interplay between a charge-density wave (CDW) phase and superconductivity. In CsV₃Sb₅, the CDW instability forms below $T_{\text{CDW}} = 94 \text{ K}^2$ (102 K for RbV₃Sb₅³ and 78 K for KV₃Sb₅¹), while superconductivity (SC) is observed below $T_c = 2.5 \text{ K}^2$ (0.92 K for RbV₃Sb₅³ and 0.93 K for KV₃Sb₅⁴).

Recently, several electrical transport, magnetic susceptibility, NMR, XRD, and μSR studies demonstrated the tunability of both orders in the AV₃Sb₅ series under external pressure^{5–17}. At low pressures ($p < 2 \text{ GPa}$), superconductivity in CsV₃Sb₅ exhibits a double-dome feature, comprising an enhancement of T_c to $\sim 7 \text{ K}$ at $p_1 \sim 0.6 \text{ GPa}$, and a second peak in T_c at $p_2 \sim 2 \text{ GPa}$ with $T_c \sim 8 \text{ K}$, whereas the superconducting gap evolves almost monotonically¹⁸. Simultaneously, T_{CDW} is gradually suppressed and vanishes at p_2 ^{5,7,10}. Experimental studies revealed a non-trivial evolution of CDW across p_1 , suggesting that changes in the nature of CDW may cause the double-dome behavior of superconductivity^{10,16,19}. For $p > 2 \text{ GPa}$, superconductivity is gradually suppressed and vanishes around 9 GPa. Surprisingly, at higher pressures ($p > 12 \text{ GPa}$), superconductivity re-emerges, with this second SC phase persisting up to at least 100 GPa^{8,11,15}. This re-entrant behavior, along with the presence of a quantum critical point (QCP) at 2 GPa, has sparked considerable debate on the superconducting pairing mechanism. Some studies propose electronic correlations at ambient pressure and CDW fluctuations around 2 GPa to be the main driving force behind the formation of Cooper pairs^{20–22}. On the other hand, first-principle calculations revealed essential

changes in electron-phonon (e-ph) coupling around the QCP, suggesting a conventional phonon-mediated mechanism^{23–26}.

The CDW state in CsV₃Sb₅ is unique within the AV₃Sb₅ series as both the $2 \times 2 \times 2$ and $2 \times 2 \times 4$ orders comprising stacked 2×2 in-plane star-of-David and trihexagonal kagome superlattices are possible at ambient pressure^{27–29}. Moreover, the experimentally observed CDW state features multiple anisotropic energy gaps^{30,31}, large anomalous Hall effect^{32,33}, intrinsic chirality^{33–35}, and a temperature-driven re-arrangement of the order parameters including an electronic nematic phase below $\sim 35 \text{ K}$ ^{16,36,37}. Some studies discuss electron-phonon coupling as the driving force behind the CDW instability in AV₃Sb₅^{24,38,39}, whereas others point towards a more complex electronic origin^{40,41}. It has been shown that band saddle points (van Hove singularities) close to the Fermi energy lead to a CDW instability in kagome metals^{42–44}, making the pressure evolution of the saddle points a potentially important ingredient for understanding the phase transformations of CsV₃Sb₅ under pressure.

Linking the pressure-induced changes in the electronic properties to modifications in the electronic band structure has been the subject of several high-pressure XRD studies, along with density functional theory calculations^{11,23–25,45–48}. The experimental confirmation of the proposed changes in the electronic band structure, however, remains lacking because the powerful ambient-pressure probes, such as ARPES and STM, are incompatible with pressure environment. Hence, we utilize high-pressure Fourier-transform infrared spectroscopy at room temperature to experimentally probe the pressure-induced modifications in the electronic structure. Assessing these changes in the normal state is crucial for understanding the changes in low-temperature instabilities of the system, because those instabilities are driven by the evolution of the electronic structure in the normal state.

¹Physikalisches Institut, Universität Stuttgart, D-70569 Stuttgart, Germany. ²Felix Bloch Institute for Solid-State Physics, Leipzig University, 04103 Leipzig, Germany. ³Experimental Physics VI, Center for Electronic Correlations and Magnetism, Institute of Physics, University of Augsburg, 86135 Augsburg, Germany. ⁴Synchrotron SOLEIL, L'Orme des Merisiers, Saint-Aubin 91192 Gif-sur-Yvette, France. ⁵Materials Department and California Nanosystems Institute, University of California Santa Barbara, Santa Barbara, CA 93106, USA. ⁶Materials Department, University of California Santa Barbara, Santa Barbara, CA 93106, USA. ⁷Helmholtz-Zentrum Dresden-Rossendorf, Institute of Ion Beam Physics and Materials Research, 01328 Dresden, Germany. ✉email: maxim.wenzel@pi1.physik.uni-stuttgart.de; altsirlin@gmail.com; e.uykur@hzdr.de

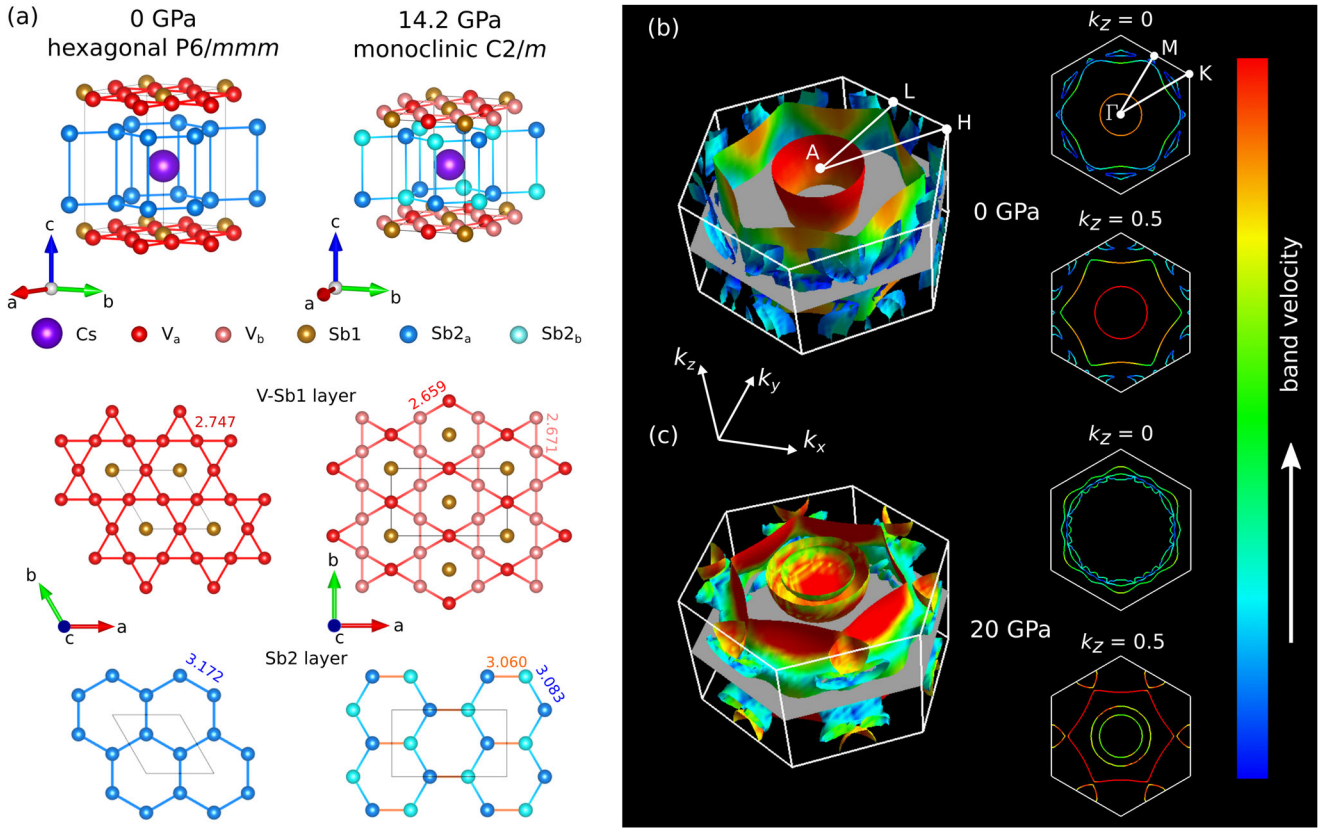


Fig. 1 Pressure evolution of the crystal structure and Fermi surface. **a** Hexagonal (left) and monoclinic (right) crystal structures of CsV_3Sb_5 as determined by XRD measurements at ambient pressure¹ and 14.2 GPa under non-hydrostatic conditions⁴⁶, respectively, visualized by VESTA⁷³. **b**, **c** Representative Fermi surfaces, at 0 and 20 GPa, respectively, created with FermiSurfer⁷⁴. Hexagonal structures⁴⁵ were used for the calculations. The color code represents the band velocity.

As most high-pressure transport measurements are performed using silicone or Daphne oil as pressure transmitting medium, increasing pressure leads to increasing non-hydrostaticity^{49,50}. It has been shown that under such conditions, CsV_3Sb_5 transforms from hexagonal to monoclinic symmetry above ~ 10 GPa⁴⁶ as sketched in Fig. 1a. The current reflectivity study has been performed with the quasi-hydrostatic CsI ⁵¹ as a pressure transmitting medium, ensuring a good sample-diamond interface, which is crucial for reliable measurements. Hence, here, a similar phase transition can also be envisaged. However, as discussed previously⁴⁶, this monoclinic distortion affects the band structure only marginally.

Our results reveal a drastic change in the interband absorption around p_2 where the CDW is suppressed. Using ab initio calculations of the band structure and optical conductivity, we show that these changes can be understood in terms of the upward shift of the Sb2 $p_x + p_y$ band and the shrinkage of the Fermi surface (FS) around the M -point. We further demonstrate that the spectral weight due to localized carriers is strongly suppressed around p_2 , suggesting the reduction in the e-ph coupling. This spectral weight is partially restored above 10 GPa, where re-entrant superconductivity is observed. Our data suggest that changes in the e-ph coupling caused by the reconstruction of the FS should be crucial for the pressure evolution of electron dynamics in CsV_3Sb_5 .

RESULTS

Intraband contributions

The decomposed real part of the in-plane optical conductivity at selected pressure points is given in Fig. 2a–d (see Supplementary

Note 2 for details on the fitting process). While the high-energy contributions ($\omega > 4000 \text{ cm}^{-1}$) are not notably affected by the applied pressure, major changes occur at low energies ($\omega < 2000 \text{ cm}^{-1}$). The optical spectrum at ambient pressure ($p = 0$ GPa), reproduced from ref. ⁵², is characterized by several interband absorptions and two clearly separated intraband contributions (i) a sharp Drude peak due to free charge carriers and (ii) an additional broad peak centered at finite frequencies corresponding to the response of localized carriers. Both of these intraband features are found to be highly sensitive to the applied pressure, as illustrated in Fig. 2e, f. Already at moderate pressures ($p < 2.3$ GPa), the intensity of the localization peak is drastically reduced and continues to decrease up to ~ 9 GPa. Upon further increasing the pressure, the localization peak becomes more pronounced again. On the other hand, the opposite trend is observed for the Drude contribution, signaling an interplay between localized and free charge carriers.

To further explore this interplay, we calculate the spectral weight (SW) by integrating the real part of the optical conductivity of the fitted Drude and localization peaks according to⁵³

$$\text{SW} = \frac{1}{\pi^2 \epsilon_0 c} \int_0^{\omega_c} \sigma_1(\omega) d\omega, \quad (1)$$

with ϵ_0 being the permittivity in vacuum and c the speed of light. The cut-off frequency is chosen as $\omega_c = 50,000 \text{ cm}^{-1}$ considering the high-energy tail of the localization peak. Figure 2g shows the pressure evolution of the Drude and localization peaks' spectral weight, as well as the total spectral weight of the intraband processes (Drude + localization peak). While the total intraband SW is found to be almost unaffected by pressure, a redistribution of spectral weight between the Drude and the localization peaks is observed.

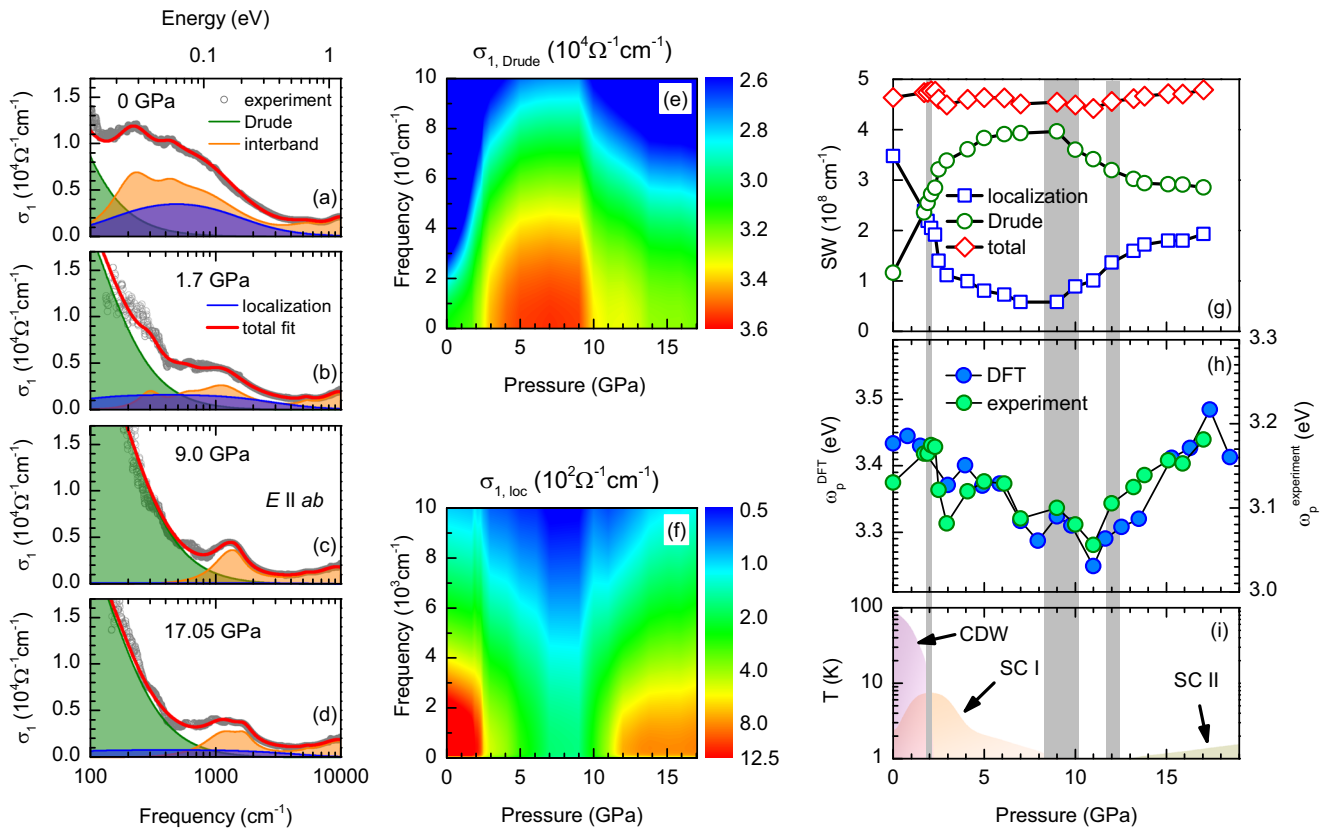


Fig. 2 Decomposition of optical conductivity and intraband spectral weight analysis. **a–d** Decomposed optical conductivity at several pressure points consisting of a Drude peak (green), a localization peak (blue), and multiple interband transitions (orange). The data at ambient pressure were taken from a previous study⁵². **e, f** Pressure evolution of the Drude and localization peaks, respectively. **g** Calculated spectral weight of the two intraband contributions (Drude and localization peaks). **h** Pressure dependence of the experimental plasma frequency deduced from the total intraband spectral weight as explained in the text and plasma frequency calculated by DFT. **i** Schematic pressure phase diagram of CsV_3Sb_5 as determined by several electrical transport, magnetic susceptibility, NMR, XRD, and μSR studies^{5–17}. The gray shaded areas mark critical pressure regions corresponding to (i) the vanishing of CDW state at ~ 2 GPa (ii) the disappearance of the first superconducting dome at around 9 GPa, and (iii) the re-emergence of superconductivity at approximately 12 GPa.

The plasma frequencies are obtained via $\omega_p = \sqrt{SW_{\text{Drude}} + SW_{\text{loc}}}$ and normalized to the value at ambient pressure from a previous study⁵² (see Supplementary Note 3 for details). As displayed in Fig. 2h, a good match between the experimental and DFT plasma frequency is observed. Here, even small features in the experimental plasma frequency like dips around 2.5 GPa, 8 GPa, and 11 GPa are well reproduced by our calculations. This good agreement between experiment and ab initio calculations over a wide pressure range suggests that electrons in CsV_3Sb_5 are almost uncorrelated, consistent with the previous assessment of the correlation strength at ambient pressure⁵². Hence, the main effect beyond the pure band picture is the damping of charge carriers manifested by the localization peak.

Interband transitions

Having discussed the intraband contributions in great detail, we now turn to analyzing the low-energy interband transitions. It has been shown that, compared to its sibling compounds, CsV_3Sb_5 possesses inverted band saddle points, leading to very different low-energy interband transitions^{52,54}. At ambient pressure, optical spectroscopy has revealed the existence of characteristic interband absorptions below 0.06 eV (marked by the red arrow in Fig. 3c), which could be well reproduced by DFT⁵².

Upon applying pressure, the experimental data show a sudden reduction of the low-energy transitions at around 0.03 eV, already at the lowest measured pressure of 1.7 GPa as depicted in Fig. 3d. This trend is corroborated by the calculated optical conductivity

plotted in Fig. 3g. Note that the difference in intensity between theoretical and experimental interband absorptions is due to the absence of electron scattering in the zero-temperature calculations. Band-resolved optical conductivity calculations displayed in Fig. 3b for 4.9 GPa, where the spectral weight below 0.06 eV is almost suppressed, reveal that these low-energy absorption arises from transitions between bands B and C according to the labeling in Fig. 3a. A closer look at the knot of bands that cross the Fermi level along Γ – M shown in Fig. 4a suggests that this part of the band structure changes significantly already at low pressures. With the $\text{Sb}2 p_x + p_y$ band becoming steeper and pushing vanadium bands above the Fermi level, several bands crossing the Fermi level disappear, and parts of the Fermi surface shrink around 3 GPa, illustrated in Fig. 4c. This effect is even better visible away from the Γ – M line (Fig. 4b), where interband transitions at 0.03–0.06 eV are clearly suppressed by pressure, and only interband transitions at $\omega > 0.1$ eV remain.

With this suppression of absorption below 0.1 eV, the experimental interband optical conductivity at low energies can be described by two absorption peaks as plotted in Fig. 3d–f. One of these peaks only slightly changes with pressure (black dotted line), while the other reveals a shift to higher energies (solid green line). This behavior is in line with our calculations showing a systematic shift of band C around the M -point away from the Fermi level, leading to a blue shift of the absorption peak related to the B–C transitions. The high consistency of the energy shift between calculations and experiment, as depicted in Fig. 3h, further supports the use of the uncorrelated band picture for the description of CsV_3Sb_5 over a broad pressure range.

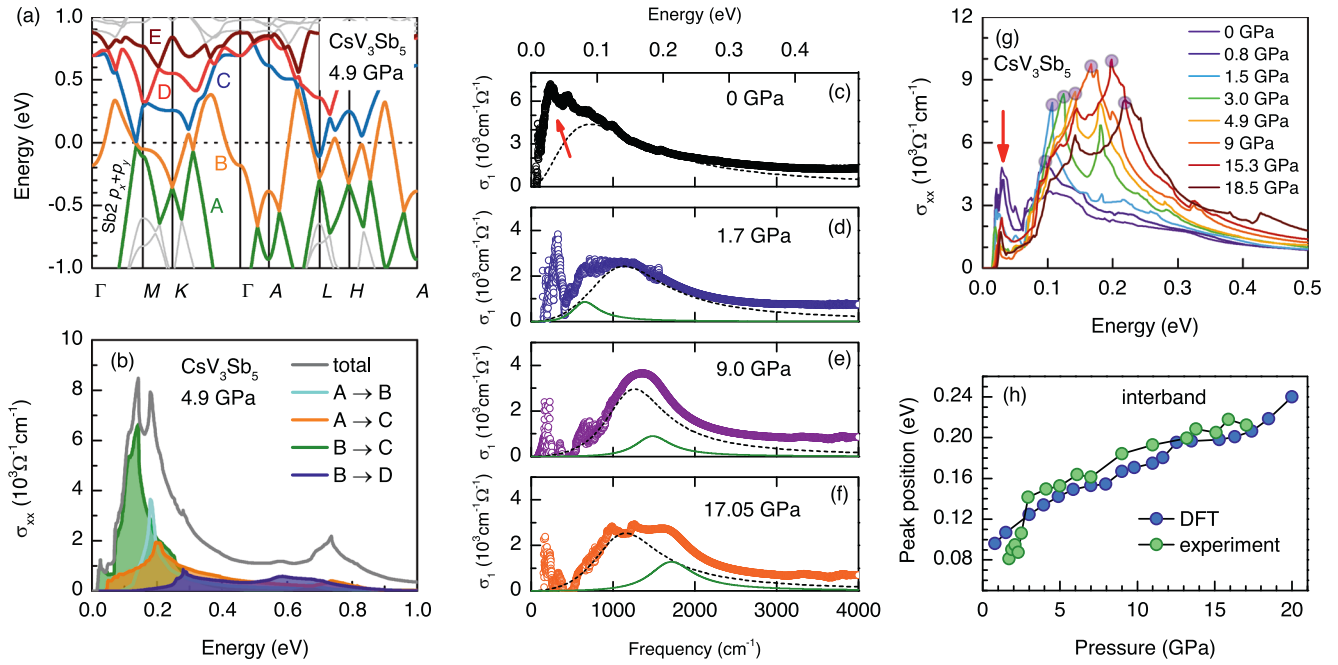


Fig. 3 Pressure evolution of the band structure and interband transitions. **a** Calculated band structure at 4.9 GPa. **b** Band-resolved contributions to the in-plane component of the calculated optical conductivity. **c–f** Experimental interband transitions at selected pressures. The red arrow marks the low-energy transitions ($\omega < 0.06$ eV) that become suppressed abruptly between 0 and 3 GPa. At low energies, the pressure data are described by two distinct absorption peaks (solid green line and black dotted line). With increasing pressure, a systematic blue shift of the green absorption is observed. **g** Pressure evolution of the calculated optical conductivity. The red arrow marks the suppression of low-energy absorption and the circles highlight the shifting interband absorption peak. **h** Pressure evolution of the blue-shifting low-energy interband absorption peak from the experimental and calculated optical conductivities.

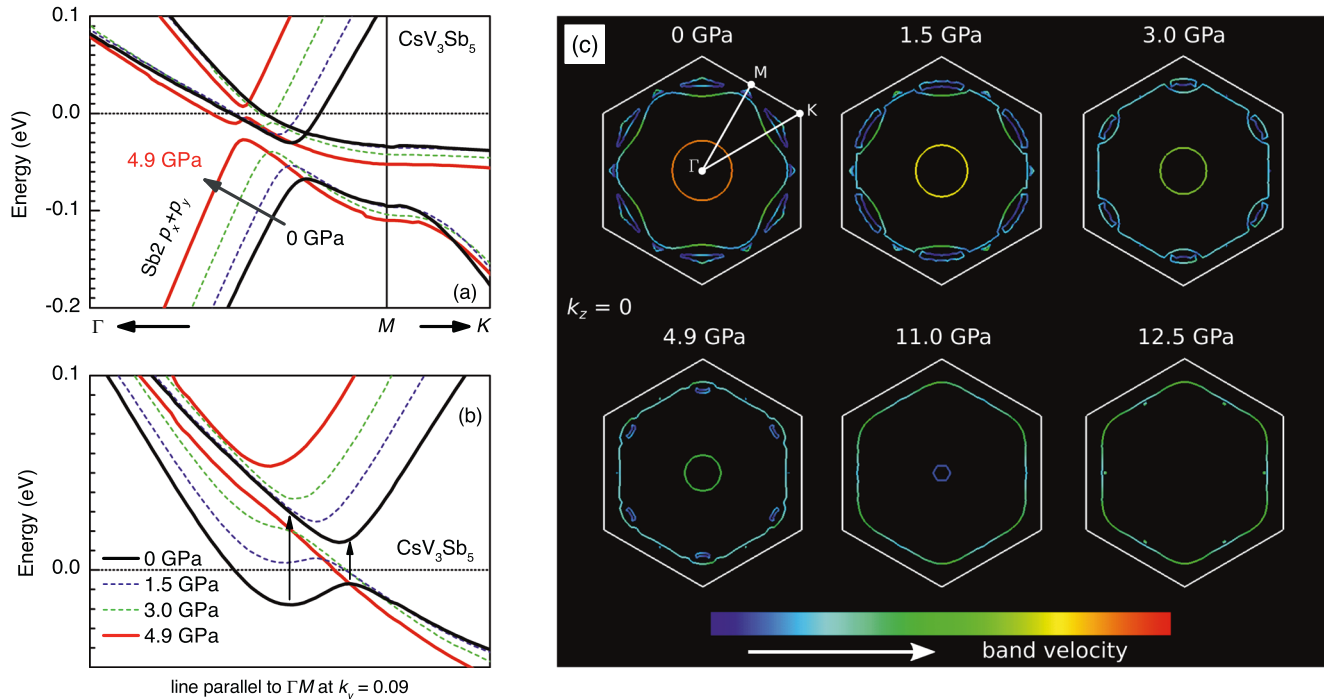


Fig. 4 Low-pressure band structures and pressure evolution of the Fermi surface. **a** Band structure along Γ - M at low pressures. **b** Band structure away from the Γ - M line shows the suppression of the low-energy interband transitions highlighted by black arrows. **c** Pressure evolution of the Fermi surface at $k_z = 0$, illustrated using FermiSurfer⁷⁴ with the band velocity as color scale.

Moreover, due to the increasing slope of the $\text{Sb2 } p_x + p_y$ band under pressure, band A comes closer to the Fermi level and even crosses it at higher pressures (see Supplementary Note 4). Consequently, the contribution of the A-B transitions

increases upon applying pressure, compared to the B-C transitions that were dominant at ambient pressure, leading to an increase of spectral weight at around 0.2 eV (see Fig. 3g).

DISCUSSION

Previously, several optical studies demonstrated a close link between the low-energy interband absorptions and fine details in the electronic band structure of the AV_3Sb_5 series^{52,54,55}. On the other hand, the localization peak, a common feature among several kagome metal compounds^{52,54–57}, can not be explained within the simple band picture. Free charge carriers interacting with low-energy degrees of freedom, such as phonons and electric or magnetic fluctuations, can lead to a backscattering of the electrons, causing localization effects manifested in a displaced Drude peak^{58,59}. In the absence of magnetism and electronic correlations, interactions between electrons and phonons become the most plausible reason for the appearance of the localization peak. This interpretation is further supported by the gradual shift of the localization peak to low energies on cooling, as phonons are suppressed⁵². Moreover, optical studies of KV_3Sb_5 and RbV_3Sb_5 find strong phonon anomalies, which are associated with the phonon modes coupling to the electronic background^{54,55}. In the magnetic rare-earth kagome metal series RMn_6Sn_6 , a close link between the behavior of phonon modes and the localization peak was also observed⁵⁶.

It is then natural to use the spectral weight of the localization peak as an experimental gauge of the electron-phonon coupling. Our data suggest that this coupling should be strongly suppressed around 2 GPa, where the CDW disappears, and T_c starts decreasing. Concurrently, the increase in the spectral weight of the localization peak above 10 GPa indicates that the e-ph coupling becomes more prominent as superconductivity reappears. On the microscopic level, first-principle calculations confirm this picture²⁴ and reveal a strong coupling of the V-V bond-stretching and V-Sb bond-bending phonon modes to the V $3d_{xy,x^2-y^2,z^2}$, V $3d_{xz,yz}$, and Sb1 $5p_z$ bands²⁶. Above 2 GPa, a drastic reduction of the coupling strength λ is proposed, corresponding to the suppression of superconductivity. Consequently, above 12 GPa, the increase of the localization peak most probably signals an increase of e-ph coupling due to the new Fermi surface around A, as displayed in Fig. 1b, c. Here, Sb2 p_z electrons appear at the Fermi level for the first time (see Supplementary Fig. 4 for the band structures at higher pressures), and probably cause the re-entrant superconductivity as illustrated in Fig. 2i. Given the unusual non-monotonic behavior of T_c under pressure, several other scenarios influencing superconductivity in CsV_3Sb_5 can be excluded. Due to only weak changes in the plasma frequency (Fig. 2h), as well as a very different pressure evolution of the electronic density of states at E_F (see Supplementary Fig. 3d), the behavior of T_c cannot be explained by modifications in the electronic structure. Moreover, the continuous evolution of the crystal structure^{45,46,48}, as well as of phonons according to previous DFT calculations^{23,24}, eliminates the Debye temperature as a dominant factor, leaving changes in the e-ph coupling as the most likely reason for the observed pressure evolution of T_c .

Apart from high-pressure investigations, CsV_3Sb_5 was subject to various doping studies^{60–66}. We would like to point out that while in some cases, for instance, through partial substitution of V-atoms with Nb-atoms, the effects on the electronic properties are similar to applying pressure, i.e., the suppression of the CDW order, along with an enhancement of T_c , doping has a somewhat different effect on the band structure. As revealed by our study, the energies of the band saddle points are only weakly affected by pressure, while the Sb2 $p_x + p_y$ bands show a significant upward shift already at moderate pressures. On the other hand, Nb-doping leads to modifications near the Γ - and M -points, highly affecting the band saddle points^{62,66}. These differences in the band structure evolution entail a distinct behavior of the low-energy interband optical transitions. The application of external pressure leads to a systematic shift of band B away from the Fermi energy around the M -point, resulting in a blue-shifting interband

absorption peak. Conversely, this low-energy absorption peak at around 400 cm^{-1} shifts to lower energies upon Nb-substitution⁶⁵.

Our study revealed that the reduction in the e-ph coupling around 2 GPa is likely the main reason for the CDW suppression in CsV_3Sb_5 . The simultaneous change in the interband absorption gives us a strong hint that this behavior is caused by the reduction of the FS along Γ - M . The Sb2 $p_x + p_y$ band, which was so far almost disregarded in the context of the CsV_3Sb_5 physics, shows an upward shift and pushes some of the V $3d$ bands above the Fermi level. This effect is qualitatively different from the scenario of band saddle points at M moving away from the Fermi level and pulling V $3d$ bands down in energy, consequently increasing the FS. We thus find a delicate interplay between electronic and lattice degrees of freedom in CsV_3Sb_5 and identify a large tunability of the kagome bands via changes in the Sb sublattice.

METHODS

Optical measurements

High-quality single crystals were grown and prepared according to ref. 1. For the optical measurements, a freshly cleaved sample with a surface area of $150\text{ }\mu\text{m} \times 150\text{ }\mu\text{m}$ and a thickness of $\sim 60\text{ }\mu\text{m}$ was used.

High-pressure reflectivity measurements were performed at room temperature at the *SMIS* beamline of the *SOLEIL* synchrotron, France, on a homemade horizontal microscope with custom Schwarzschild objectives ($NA = 0.5$). A diamond anvil cell (DAC) with type-IIa diamond anvils and a culet of $400\text{ }\mu\text{m}$ diameter was utilized. Finely ground CsI powder served as the pressure transmitting medium, making it possible to reach pressures up to 17.05 GPa. The sample and Ruby spheres used as pressure gauges were placed inside a stainless steel gasket with a $200\text{ }\mu\text{m}$ diameter hole. The pressure was determined by monitoring the calibrated shift of the ruby R1 fluorescence line as described in ref. 67.

The reflectivity spectra at the sample-diamond interface were recorded in a broad spectral range of 150 – $10,000\text{ cm}^{-1}$ by a Thermo-Fisher iS50 interferometer with KBr and solid substrate beamsplitters, using a MCT detector and a liquid helium-cooled bolometer. The reflectivity of a gold foil loaded into the DAC at ambient pressure served as a reference. Other optical quantities like the complex optical conductivity $\tilde{\sigma}(\omega)$, or the dielectric permittivity $\tilde{\epsilon}(\omega)$, were obtained using standard Kramers-Kronig (KK) analysis considering the sample-diamond interface as explained in Supplementary Note 1.

Computational details

Density-functional (DFT) band-structure calculations were performed with the *Wien2K* code^{68,69} and cross-checks have been conducted with the *FPLM* code⁷⁰. In all cases, the Perdew-Burke-Ernzerhof flavor of the exchange-correlation potential⁷¹ was used, and self-consistent calculations were converged on the k -mesh with $24 \times 24 \times 12$ points. Experimental crystal structural parameters from refs. 1,45 were used. Considering that the monoclinic distortion does not have a fundamental impact on the band structure⁴⁶, we used hexagonal structure throughout the pressure range for a simpler comparison. Optical conductivity was calculated using the *optic* module⁷² on the dense k -mesh with up to $100 \times 100 \times 50$ points. Spin-orbit coupling was included in all the calculations.

DATA AVAILABILITY

The data that support the findings of this study are available from the corresponding authors upon request.

Received: 28 April 2023; Accepted: 18 August 2023;

Published online: 01 September 2023

REFERENCES

- Ortiz, B. R. et al. New kagome prototype materials: discovery of KV_3Sb_5 , RbV_3Sb_5 , and CsV_3Sb_5 . *Phys. Rev. Mater.* **3**, 094407 (2019).
- Ortiz, B. R. et al. CsV_3Sb_5 : a \mathbb{Z}_2 topological kagome metal with a superconducting ground state. *Phys. Rev. Lett.* **125**, 247002 (2020).
- Yin, Q. et al. Superconductivity and normal-state properties of kagome metal RbV_3Sb_5 single crystals. *Chin. Phys. Lett.* **38**, 037403 (2021).
- Ortiz, B. R. et al. Superconductivity in the \mathbb{Z}_2 kagome metal KV_3Sb_5 . *Phys. Rev. Mater.* **5**, 034801 (2021).
- Chen, K. Y. et al. Double superconducting dome and triple enhancement of T_c in the kagome superconductor CsV_3Sb_5 under high pressure. *Phys. Rev. Lett.* **126**, 247001 (2021).
- Wang, Q. et al. Charge density wave orders and enhanced superconductivity under pressure in the kagome metal CsV_3Sb_5 . *Adv. Mater.* **33**, 2102813 (2021).
- Yu, F. H. et al. Unusual competition of superconductivity and charge-density-wave state in a compressed topological kagome metal. *Nat. Commun.* **12**, 3645 (2021).
- Zhao, C. C. et al. Nodal superconductivity and superconducting dome in the topological Kagome metal CsV_3Sb_5 . Preprint at <https://arxiv.org/abs/2102.08356> (2021).
- Zhu, C. C. et al. Double-dome superconductivity under pressure in the V-based kagome metals AV_3Sb_5 ($A = Rb$ and K). *Phys. Rev. B* **105**, 094507 (2022).
- Li, H. et al. Discovery of conjoined charge density waves in the kagome superconductor CsV_3Sb_5 . *Nat. Commun.* **13**, 6348 (2022).
- Chen, X. et al. Highly robust reentrant superconductivity in CsV_3Sb_5 under pressure. *Chin. Phys. Lett.* **38**, 057402 (2021).
- Guguchia, Z. et al. Tunable unconventional kagome superconductivity in charge ordered RbV_3Sb_5 and KV_3Sb_5 . *Nat. Commun.* **14**, 153 (2023).
- Wang, N. N. et al. Competition between charge-density-wave and superconductivity in the kagome metal RbV_3Sb_5 . *Phys. Rev. Res.* **3**, 043018 (2021).
- Du, F. et al. Pressure-induced double superconducting domes and charge instability in the kagome metal KV_3Sb_5 . *Phys. Rev. B* **103**, L220504 (2021).
- Zhang, Z. et al. Pressure-induced reemergence of superconductivity in the topological kagome metal CsV_3Sb_5 . *Phys. Rev. B* **103**, 224513 (2021).
- Zheng, L. et al. Emergent charge order in pressurized kagome superconductor CsV_3Sb_5 . *Nature* **611**, 682–687 (2022).
- Gupta, R. et al. Two types of charge order with distinct interplay with superconductivity in the kagome material CsV_3Sb_5 . *Commun. Phys.* **5**, 232 (2022).
- Wen, X. et al. Emergent superconducting fluctuations in compressed kagome superconductor CsV_3Sb_5 . *Sci. Bull.* **68**, 259–265 (2023).
- Feng, X. Y. et al. Commensurate-to-incommensurate transition of charge-density-wave order and a possible quantum critical point in pressurized kagome metal CsV_3Sb_5 . Preprint at <https://arxiv.org/abs/2303.01225> (2023).
- Neupert, T., Denner, M. M., Yin, J.-X., Thomale, R. & Hasan, M. Z. Charge order and superconductivity in kagome materials. *Nat. Phys.* **18**, 137–143 (2022).
- Wu, X. et al. Nature of unconventional pairing in the kagome superconductors AV_3Sb_5 ($A = K, Rb, Cs$). *Phys. Rev. Lett.* **127**, 177001 (2021).
- Tazai, R., Yamakawa, Y., Onari, S. & Kontani, H. Mechanism of exotic density-wave and beyond-Migdal unconventional superconductivity in kagome metal AV_3Sb_5 ($A = K, Rb, Cs$). *Sci. Adv.* **8**, eabl4108 (2022).
- Zhang, J.-F., Liu, K. & Lu, Z.-Y. First-principles study of the double-dome superconductivity in the kagome material CsV_3Sb_5 under pressure. *Phys. Rev. B* **104**, 195130 (2021).
- Si, J.-G., Lu, W.-J., Sun, Y.-P., Liu, P.-F. & Wang, B.-T. Charge density wave and pressure-dependent superconductivity in the kagome metal CsV_3Sb_5 : a first-principles study. *Phys. Rev. B* **105**, 024517 (2022).
- Wang, C., Liu, S., Jeon, H., Jia, Y. & Cho, J.-H. Charge density wave and superconductivity in the kagome metal CsV_3Sb_5 around a pressure-induced quantum critical point. *Phys. Rev. Mater.* **6**, 094801 (2022).
- Wang, C., Yu, J., Zhang, Z. & Cho, J.-H. Phonon-mediated S-wave superconductivity in the kagome metal CsV_3Sb_5 under pressure. Preprint at <https://arxiv.org/abs/2303.10080> (2023).
- Ortiz, B. R. et al. Fermi surface mapping and the nature of charge-density-wave order in the kagome superconductor CsV_3Sb_5 . *Phys. Rev. X* **11**, 041030 (2021).
- Hu, Y. et al. Coexistence of trihexagonal and star-of-David pattern in the charge density wave of the kagome superconductor AV_3Sb_5 . *Phys. Rev. B* **106**, L241106 (2022).
- Kang, M. et al. Charge order landscape and competition with superconductivity in kagome metals. *Nat. Mater.* **22**, 186–193 (2022).
- Wang, Z. et al. Distinctive momentum dependent charge-density-wave gap observed in CsV_3Sb_5 superconductor with topological Kagome lattice. Preprint at <https://arxiv.org/abs/2104.05556> (2021).
- Nakayama, K. et al. Multiple energy scales and anisotropic energy gap in the charge-density-wave phase of the kagome superconductor CsV_3Sb_5 . *Phys. Rev. B* **104**, L161112 (2021).
- Yu, F.-H. et al. Pressure tuning of the anomalous Hall effect in the kagome superconductor CsV_3Sb_5 . *Chin. Phys. B* **31**, 017405 (2022).
- Yu, F. H. et al. Concurrence of anomalous Hall effect and charge density wave in a superconducting topological kagome metal. *Phys. Rev. B* **104**, L041103 (2021).
- Wang, Z. et al. Electronic nature of chiral charge order in the kagome superconductor CsV_3Sb_5 . *Phys. Rev. B* **104**, 075148 (2021).
- Guo, C. et al. Switchable chiral transport in charge-ordered kagome metal CsV_3Sb_5 . *Nature* **611**, 461–466 (2022).
- Nie, L. et al. Charge-density-wave-driven electronic nematicity in a kagome superconductor. *Nature* **604**, 59–64 (2022).
- Stahl, Q. et al. Temperature-driven reorganization of electronic order in CsV_3Sb_5 . *Phys. Rev. B* **105**, 195136 (2022).
- Xie, Y. et al. Electron-phonon coupling in the charge density wave state of CsV_3Sb_5 . *Phys. Rev. B* **105**, L140501 (2022).
- Luo, H. et al. Electronic nature of charge density wave and electron-phonon coupling in kagome superconductor KV_3Sb_5 . *Nat. Commun.* **13**, 273 (2022).
- Tan, H., Liu, Y., Wang, Z. & Yan, B. Charge density waves and electronic properties of superconducting kagome metals. *Phys. Rev. Lett.* **127**, 046401 (2021).
- Li, H. et al. Observation of unconventional charge density wave without acoustic phonon anomaly in kagome superconductors AV_3Sb_5 ($A = Rb, Cs$). *Phys. Rev. X* **11**, 031050 (2021).
- Kiesel, M. L., Platt, C. & Thomale, R. Unconventional fermi surface instabilities in the kagome Hubbard Model. *Phys. Rev. Lett.* **110**, 126405 (2013).
- Park, T., Ye, M. & Balents, L. Electronic instabilities of kagome metals: Saddle points and Landau theory. *Phys. Rev. B* **104**, 035142 (2021).
- Denner, M. M., Thomale, R. & Neupert, T. Analysis of charge order in the kagome metal AV_3Sb_5 ($A = K, Rb, Cs$). *Phys. Rev. Lett.* **127**, 217601 (2021).
- Tsirlin, A. A. et al. Role of Sb in the superconducting kagome metal CsV_3Sb_5 revealed by its anisotropic compression. *SciPost Phys.* **12**, 49 (2022).
- Tsirlin, A. A. et al. Effect of nonhydrostatic pressure on the superconducting kagome metal CsV_3Sb_5 . *Phys. Rev. B* **107**, 174107 (2023).
- LaBollita, H. & Botana, A. S. Tuning the Van Hove singularities in AV_3Sb_5 ($A = K, Rb, Cs$) via pressure and doping. *Phys. Rev. B* **104**, 205129 (2021).
- Yu, F. et al. Pressure-induced dimensional crossover in a kagome superconductor. *Phys. Rev. Lett.* **128**, 077001 (2022).
- Klotz, S., Chervin, J.-C., Munsch, P. & Marchand, G. L. Hydrostatic limits of 11 pressure transmitting media. *J. Phys. D: Appl. Phys.* **42**, 075413 (2009).
- Santamaría-Pérez, D. et al. High-pressure study of the behavior of mineral barite by x-ray diffraction. *Phys. Rev. B* **84**, 054102 (2011).
- Celeste, A., Borondics, F. & Capitani, F. Hydrostaticity of pressure-transmitting media for high pressure infrared spectroscopy. *High. Press. Res.* **39**, 608–618 (2019).
- Uykur, E. et al. Low-energy optical properties of the nonmagnetic kagome metal CsV_3Sb_5 . *Phys. Rev. B* **104**, 045130 (2021).
- Dressel, M. & Grüner, G. *Electrodynamics of Solids: Optical Properties of Electrons in Matter* (Cambridge University Press, 2002).
- Wenzel, M. et al. Optical study of RbV_3Sb_5 : multiple density-wave gaps and phonon anomalies. *Phys. Rev. B* **105**, 245123 (2022).
- Uykur, E., Ortiz, B. R., Wilson, S. D., Dressel, M. & Tsirlin, A. A. Optical detection of the density-wave instability in the kagome metal KV_3Sb_5 . *npj Quantum Mater.* **7**, 16 (2022).
- Wenzel, M. et al. Effect of magnetism and phonons on localized carriers in the ferrimagnetic kagome metals $GdMn_6Sn_6$ and $TbMn_6Sn_6$. *Phys. Rev. B* **106**, L241108 (2022).
- Biswas, A. et al. Spin-reorientation-induced band gap in Fe_3Sn_2 : optical signatures of weyl nodes. *Phys. Rev. Lett.* **125**, 076403 (2020).
- Fratini, S., Ciuchi, S. & Mayou, D. Phenomenological model for charge dynamics and optical response of disordered systems: application to organic semiconductors. *Phys. Rev. B* **89**, 235201 (2014).
- Fratini, S. & Ciuchi, S. Displaced Drude peak and bad metal from the interaction with slow fluctuations. *SciPost Phys.* **11**, 039 (2021).
- Xiao, Q. et al. Evolution of charge density waves from three-dimensional to quasi-two-dimensional in kagome superconductors $Cs(V_{1-x}M_x)_3Sb_5$ ($M = Nb, Ta$). *Phys. Rev. Mater.* **7**, 074801 (2023).
- Oey, Y. M. et al. Fermi level tuning and double-dome superconductivity in the kagome metal $CsV_3Sb_{5-x}Sn_x$. *Phys. Rev. Mater.* **6**, L041801 (2022).
- Li, Y. et al. Tuning the competition between superconductivity and charge order in the kagome superconductor $Cs(V_{1-x}Nb_x)_3Sb_5$. *Phys. Rev. B* **105**, L180507 (2022).

63. Liu, M. et al. Evolution of superconductivity and charge density wave through Ta and Mo doping in CsV_3Sb_5 . *Phys. Rev. B* **106**, L140501 (2022).
64. Song, Y. et al. Competition of superconductivity and charge density wave in selective oxidized CsV_3Sb_5 thin flakes. *Phys. Rev. Lett.* **127**, 237001 (2021).
65. Zhou, X. et al. Effects of niobium doping on the charge density wave and electronic correlations in the kagome metal $\text{Cs}(\text{V}_{1-x}\text{Nb}_x)_3\text{Sb}_5$. *Phys. Rev. B* **107**, 125124 (2023).
66. Kato, T. et al. Fermiology and Origin of T_c enhancement in a kagome superconductor $\text{Cs}(\text{V}_{1-x}\text{Nb}_x)_3\text{Sb}_5$. *Phys. Rev. Lett.* **129**, 206402 (2022).
67. Mao, H. K., Xu, J. & Bell, P. M. Calibration of the ruby pressure gauge to 800 kbar under quasi-hydrostatic conditions. *J. Geophys. Res. Solid Earth* **91**, 4673–4676 (1986).
68. Blaha, P. et al. *WIEN2k: an augmented plane wave plus local orbitals program for calculating crystal properties* (Techn. Universitat, 2019).
69. Blaha, P. et al. WIEN2k: an APW+lo program for calculating the properties of solids. *J. Chem. Phys.* **152**, 074101 (2020).
70. Koepnick, K. & Eschrig, H. Full-potential nonorthogonal local-orbital minimum-basis band-structure scheme. *Phys. Rev. B* **59**, 1743–1757 (1999).
71. Perdew, J. P., Burke, K. & Ernzerhof, M. Generalized gradient approximation made simple. *Phys. Rev. Lett.* **77**, 3865–3868 (1996).
72. Ambrosch-Draxl, C. & Sofo, J. O. Linear optical properties of solids within the full-potential linearized augmented planewave method. *Comput. Phys. Commun.* **175**, 1–14 (2006).
73. Momma, K. & Izumi, F. VESTA: a three-dimensional visualization system for electronic and structural analysis. *J. Appl. Crystallogr.* **41**, 653–658 (2008).
74. Kawamura, M. FermiSurfer: Fermi-surface viewer providing multiple representation schemes. *Comput. Phys. Commun.* **239**, 197–203 (2019).

ACKNOWLEDGEMENTS

We are grateful to Gabriele Untereiner for preparing the single crystals for the optical measurements. We thank SOLEIL synchrotron, France, for providing the beamtime (proposal No. 20210399). M.W. is supported by IQST Stuttgart/Ulm via a project funded by Carl Zeiss foundation. S.D.W. and B.R.O. gratefully acknowledge support via the UC Santa Barbara NSF Quantum Foundry funded via the Q-AMASE-i program under award DMR-1906325. B.R.O. also acknowledges support from the California NanoSystems Institute through the Elings fellowship program. The work has been supported by the Deutsche Forschungsgemeinschaft (DFG) via DR228/51-3 and UY63/2-1. E.U. acknowledges the European Social Fund and the Baden-Württemberg Stiftung for the financial support of this research project by the Eliteprogramme. Computations for this work were done (in part) using resources of the Leipzig University Computing Center.

AUTHOR CONTRIBUTIONS

M.W., E.U. and Y.T.C. performed the experiments with technical support from F.C. A.A.T. performed the DFT calculations. The samples were grown by B.R.O. and S.D.W. The manuscript was written by M.W., E.U., A.A.T., and M.D. with suggestions from all authors.

FUNDING

Open Access funding enabled and organized by Projekt DEAL.

COMPETING INTERESTS

The authors declare no competing interests.

ADDITIONAL INFORMATION

Supplementary information The online version contains supplementary material available at <https://doi.org/10.1038/s41535-023-00577-4>.

Correspondence and requests for materials should be addressed to Maxim Wenzel, Alexander A. Tsirlin or Ece Uykur.

Reprints and permission information is available at <http://www.nature.com/reprints>

Publisher's note Springer Nature remains neutral with regard to jurisdictional claims in published maps and institutional affiliations.



Open Access This article is licensed under a Creative Commons Attribution 4.0 International License, which permits use, sharing, adaptation, distribution and reproduction in any medium or format, as long as you give appropriate credit to the original author(s) and the source, provide a link to the Creative Commons license, and indicate if changes were made. The images or other third party material in this article are included in the article's Creative Commons license, unless indicated otherwise in a credit line to the material. If material is not included in the article's Creative Commons license and your intended use is not permitted by statutory regulation or exceeds the permitted use, you will need to obtain permission directly from the copyright holder. To view a copy of this license, visit <http://creativecommons.org/licenses/by/4.0/>.

© The Author(s) 2023